Renewable Energy 102 (2017) 65–76

Contents lists available at ScienceDirect

Renewable Energy

journal homepage: www.elsevier.com/locate/renene

# Modelling study of the effects of suspended aquaculture installations on tidal stream generation in Cobscook Bay

Fearghal O'Donncha [a, *], Scott C. James [b], Emanuele Ragnoli [a]

[a] Constrained Resources and Environmental Analytics, IBM Research, Dublin, Ireland
[b] Department of Geology and Mechanical Engineering, Baylor University, Waco, TX, USA

ARTICLE INFO

*Article history:*
Received 23 February 2016
Received in revised form
12 September 2016
Accepted 13 October 2016
Available online 18 October 2016

*Keywords:*
Numerical modelling
Aquaculture
Tidal energy
EFDC

ABSTRACT

Recent endeavours have focused on the possibility of developing multi-use marine areas that integrate aquaculture with marine renewable energy device deployment. This work investigates both the individual and the combined impacts of suspended long-line mussel farms (canopies) and tidal stream devices. An amended version of an existing three-dimensional hydro-environmental code was used to describe the effects of both the aquaculture canopies and the tidal energy devices. The model was applied to a designated tidal energy test site on the East Coast of the United States, Cobscook Bay, ME. The quantifiable energy production capacity of the tidal stream devices with and without suspended canopies was considered. The effects of both types of structures on hydrodynamics and solute transport were analysed including flushing studies to quantify renewal timescales in the bay. Results demonstrate potential to optimise energy generation by combining turbine arrays with suspended aquaculture canopies. Combining MHK and aquaculture installations did not significantly impact the physical environment beyond the effects of the aquaculture canopies alone. Moreover, the potential energy production capacity was increased by up to 19% due to flow diversion and acceleration induced by the aquaculture canopies.



## 1. Introduction

Global aquaculture has grown dramatically over the past 50 years to 66.6 million tonnes (in 2014), worth US$106 billion and accounting for around 42% of the world's fish food supply [1]. This expansion makes aquaculture the fastest growing food production sector on the planet with an annual growth rate of 6.2%, leading to hopes of a “Blue Revolution” that matches the “Green Revolution” of higher grain yields from the 1950s onward [2]. Concurrently, increases in global energy demands and decreases in fossil fuel reserves have the world's population turning to renewable energies like tidal power, which is attractive as a predictable renewable source due to the deterministic nature of tides. Because of environmental considerations and stakeholders concerns, both these industries are tending to move further offshore to reduce spatial constraints, increase production capacity, and reduce potentially adverse environmental impacts [3].

Recent endeavours have focused on the possibility of developing multi-use marine areas that integrate open-ocean aquaculture in conjunction with marine renewable energy devices [4]. Advantages of performing mariculture activities within offshore tidal energy arrays are manifold. Placement of mariculture infrastructure above tidal turbines reduces project footprints through multiple use of ocean territories [5], while infrastructure for regular servicing may be shared. Both industries require multi-use sources of transportation, preferably with lifting capacities to install and change components. This affords an opportunity for both enterprises to share these high-priced assets [6]. Also, there are options to link individual activities of both industries, for example, harvesting in conjunction with scheduled turbine maintenance [3]. Clearly, there are many opportunities to develop these facilities in tandem while providing a range of practical advantages. However, little is known about the potential effects of these operations in coastal regions, or of the cumulative impacts on aquatic ecosystems over years or decades of operation. Both installations impact local hydrodynamics by acting as physical obstacles to flow, thereby reducing water velocities within developed areas [7–9]. Currents are key agents for both industries, impacting transport of nutrients and wastes from fish species, while current speeds dictate the energy

* Corresponding author.
*E-mail address:* feardonn@ie.ibm.com (F. O'Donncha).

http://dx.doi.org/10.1016/j.renene.2016.10.024
0960-1481/

generating capacity of MHK devices.

This work presents numerical modelling studies of the impacts of suspended aquaculture farms and MHK-device deployments on flows and material transport. The study adopts an amended version of an existing three-dimensional hydro-environmental code, Environmental Fluid Dynamics Code (EFDC) [10], to describe the effects of these structures. The effects of the suspended canopies are simulated using a laboratory-validated, vertically varying drag coefficient profile within the canopy, along with a two-equation turbulence closure scheme, which includes additional turbulent production and dissipation terms [11,12]. An MHK module considers energy removal from MHK devices and commensurate changes to turbulent kinetic energy and turbulent kinetic energy dissipation [13–16].

The energy-production capacity of tidal-stream devices with and without the suspended canopy is investigated. The research seeks the optimum configuration and density of suspended shellfish cultivation that provides viable growth conditions while maintaining or increasing energy-generation capacity of the tidal energy arrays. Emphasis is placed on the optimal configuration of both installations to promote synergistic interactions. The environmental effects of these industry developments are also investigated. In the following sections, the methodology adopted is outlined, which discusses the numerical model and the amendment of the governing equations to represent impeded flows. The Results section presents findings from case study deployments in Cobscook Bay. Finally, the conclusions from this research are presented and future work is discussed.

## 2. Methodology

### 2.1. Model configuration

The model used for this study was EFDC, a three-dimensional, finite difference, hydrodynamic model. An outline of this model is presented here and the reader is referred to Hamrick [10,17], and Ji et al. [18], for a detailed description of the numerical algorithm.

EFDC is a general-purpose modelling package for simulating three-dimensional flow, transport and biogeochemical processes in surface water systems. It resolves the vertically hydrostatic momentum and continuity equations in a curvilinear coordinates system, orthogonal in the horizontal and sigma-stretched, or terrain-following in the vertical. Three dimensional transport equations for temperature, salinity, dye tracer and suspended sediment are also computed simultaneously. A second-order turbulence closure model developed by Mellor and Yamada [19] and modified by Galperin et al. [20] is adopted to provide the vertical turbulent viscosity in the model. Horizontal diffusion is calculated via the Smagorinsky formula [21]. The code is parallelized using a domain decomposition approach with MPI synchronization between domains [22,23], while research is ongoing on provisioning via a Cloud offering [24,25].

Specifically designed to simulate estuaries and subestuarine components (tributaries, marshes, wet and dry littoral margins), the model has been used in large number of environmental studies in the Chesapeake Bay region [26]. It has also been applied in a wide range of investigations of other systems including: environmental impact assessment studies [27], suspended sediment transport [28,29], water quality [30,31] and hydrothermal responses [32]. The model is presently being used by universities, research organisations, governmental agencies, and consulting firms [33].

The model was applied to Cobscook Bay, located at the mouth of the Bay of Fundy in Maine, USA. The bay is about 10 km long and 10 km wide and has a long, convoluted coastline with many islands. From west to east, the bay is commonly divided into the inner, central, and outer bay, which are connected via a narrow channel. The Cobscook Bay region is well known for its vigorous tidal currents, abundant ocean production, and diverse ecosystem [34]. The resulting high current velocities and suitable temperatures make aquaculture an important industry in the bay [35]. Further, because of its large tidal range and nearly enclosed nature, the region has obvious potential as a site for tidal-power generation [36].

The Cobscook Bay model was developed with Cartesian $100 \times 100$ m$^2$ cells and 40 sigma layers. The model includes very high resolution in the vertical to accurately parameterise vertical shear gradients resulting from the aquaculture and MHK installations. Bathymetric data were downloaded from National Oceanographic & Atmospheric Administration (NOAA) National Geophysical Data Center server, specifically data sets H12257, H12258, and H12259 collected in 2010. The survey data was at a horizontal resolution of 2 m [37] and were then interpolated onto the model cells using the nearest neighbour technique with results shown in Fig. 1.

The open sea boundary of the model was specified at the Eastern boundary (denoted by blue cells in Fig. 1). There are two types of hydrodynamic open boundary conditions (OBC) available within the EFDC model [17]. The first type uses the standard specification of water surface elevations, using combinations of harmonic constituents and time series. The second type uses the radiation-separation boundary condition [38]. With this type of OBC, the incoming wave at an open boundary is separated from the outgoing wave and the incident wave is assumed to be twice the surface elevation required [39]. In this study, the first type of boundary condition was used, with the boundaries being treated as open boundaries and with water levels being specified. Data was collected at Eastport, Maine [40], which provides real-time tidal data at 6 min intervals. This collection point is less than 2 km from the actual model boundary.

### 2.2. Model verification

Using the Eastport water-level data to drive the model (July 6$^{th}$–30$^{th}$, 2004), various comparisons were made at the three locations where water-level data are available from NOAA (Garnet, Coffin, and Gravelly Points, see Fig. 1). Cross-correlation plots of the EFDC water levels ($x$ axis) and the NOAA data ($y$ axis) for Garnet

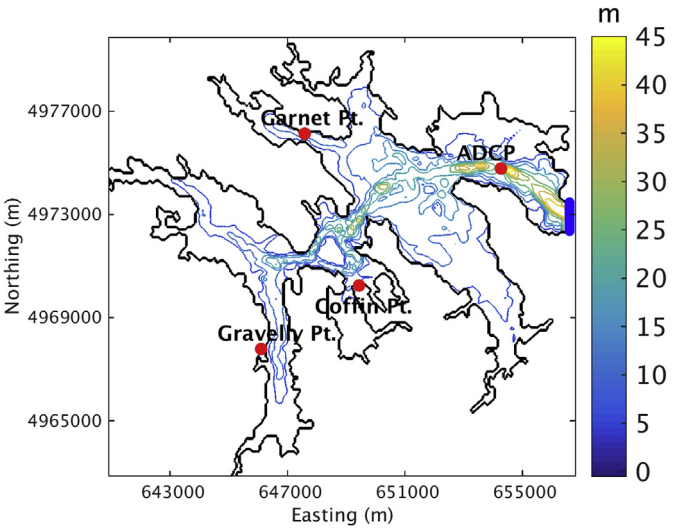


**Fig. 1.** Cobscook Bay bathymetry showing locations of water-level collection stations and ADCP deployment site. The blue cells on the eastern side represent the inlet boundary location.

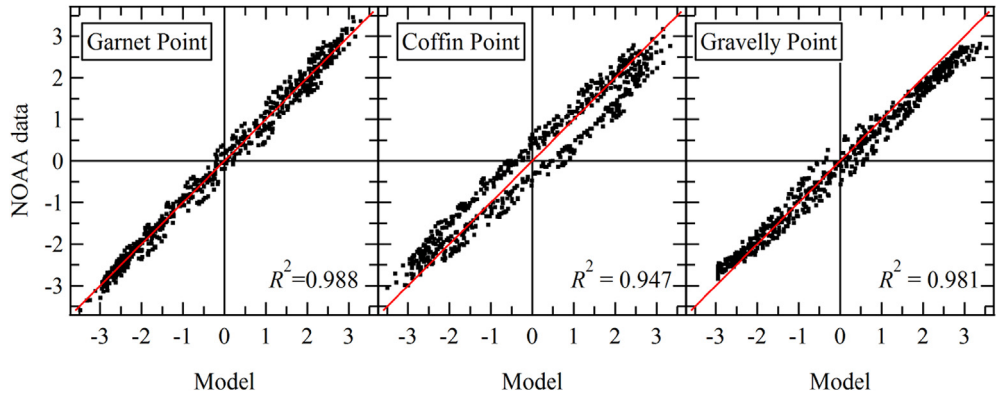


**Fig. 2.** Cross-correlation between model computed water elevations and NOAA data for Garnet Point (left), Coffin Point (center) and Gravelly Point (right).

(left), Coffin (center), and Gravelly (right) Points are shown in Fig. 2. Red lines represent the one-to-one correlation indicating a perfect match between model and data. The correlation coefficients are listed on the plots and they demonstrate very close agreement between model and data. Slopes less than unity for the fit to the cross-correlation data indicate that the model tends to over-predict water levels for Coffin and Gravelly Points (slopes of 0.87 and 0.86, respectively, indicate about 13% and 14% over-predictions). The oval-shape trend in cross-correlations for Coffin Point indicates that there is a small phase shift between the model and data. It is worth noting that modelling from the University of Maine that used only tidal and wind forcing showed good agreement with available depth, velocity, and tracer data near Cobscook Bay [41]. Conclusions from that work indicate that temperature, and density gradients are not critical factors influencing hydrodynamic circulation in the bay.

Acoustic Doppler Current Profiler (ADCP) data were collected by the Ocean Renewable Power Corporation (ORPC) from July 5th through August 5th, 2011, (the ADCP location is shown on Fig. 1). Measured water-level data for this timeframe at Eastport were again used to drive the model and model validation focused on agreement with the ADCP data for the 30 day period. Fig. 3 compares ADCP data to EFDC model results for depth-averaged water speed. EFDC under predicts the ADCP data by about 5% on average over the period of record. In agreement with what was reported by Rao et al. [42], the phase and trend of the speeds are consistent between data and model, but the magnitude is under predicted.

Fig. 4 presents a scatter plot from the model-data comparisons. The cross-correlation plot of model to ADCP speeds is shown in Fig. 4(a). The red line shows the one-to-one correlation. The correlation coefficient ($R^2 = 0.717$) is lower for the speed data than for the water-level data indicating more variability between the model and data, but there is not a large bias as the data are fairly symmetric about the one-to-one line. In fact, the best fit line to the correlation data has slope 1.05 suggesting that the model under-predicts the ADCP data by about 5%.

An absolute measure of model deviation from measured data is the root-mean-square deviation (RMSD) which can be expressed as:

$$RMSD = \sqrt{\frac{\sum_{i=1}^{n} (X_{model} - X_{obs})^2}{n}} \tag{1}$$

where $X_{model}$ and $X_{obs}$ represent the predicted and observed value respectively. An RMSD of 0.25 m/s was computed for this ADCP deployment. This corresponds to a relative RMSD (defined as the RMSD divided by the data range [33]) of 13% indicating reasonably strong agreement between model and measurements.

The ability of a model to predict events is often too elusive to be adequately encapsulated by these standardised coefficients of agreement [43]. In particular, performance metrics are very sensitive to small changes in phase, and periods of the tidal cycle when the flow speeds are low (which can generate high relative errors). In order to circumvent these difficulties, Willmott [44] proposed a model skill score, $d$, to overcome the sensitivity of correlation statistics to differences in the predicted mean and variances [45]. It can be expressed as:

$$d = 1 - \frac{\sum \left| X_{model} - X_{obs} \right|^2}{\sum \left( \left| X_{model} - \overline{X}_{obs} \right| + \left| X_{obs} - \overline{X}_{obs} \right| \right)^2} \tag{2}$$

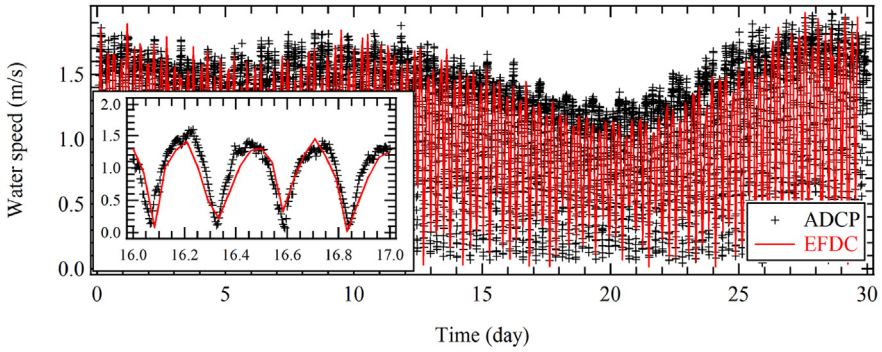


**Fig. 3.** Comparison of ADCP (symbols) to EFDC (red curves) velocities. (For interpretation of the references to colour in this figure legend, the reader is referred to the web version of this article.)

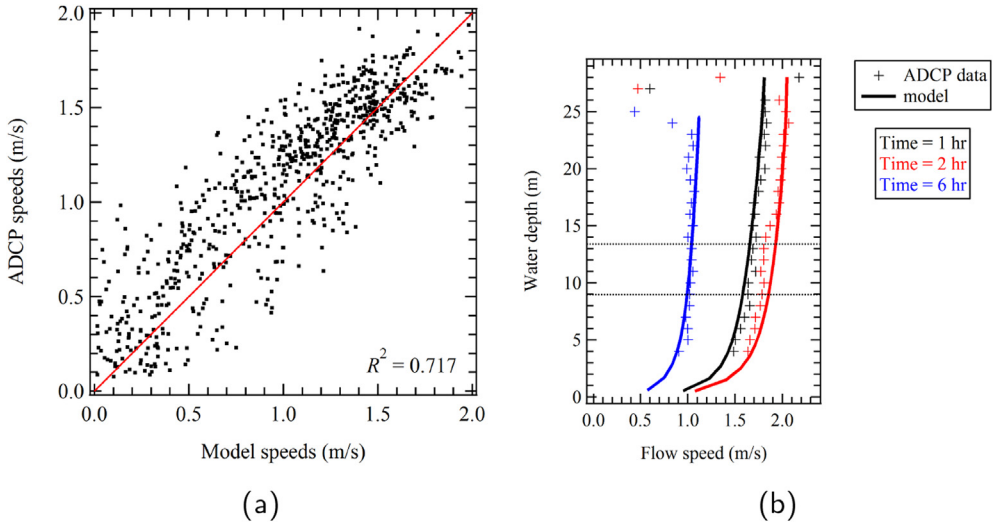


**Fig. 4.** (a) Cross-correlation plot of model and ADCP average speeds. (b) Snapshots of the vertical velocity profile from ADCP data (symbols) and EFDC (curves). The dashed lines show the approximate elevation of the MHK turbine. The velocity profiles do not reflect the presence of a turbine.

where the overbar denotes the mean of the dataset. The highest value, $d = 1$, means perfect agreement between model and observation, while the lowest, $d = 0$, indicates complete disagreement. Skill scores permit greater insights into the predictive abilities of models with allowances for ambient flow speeds and relative RMSD. In assessing model performance Legates and McCabe [45] recommends the inclusion of at least one relative error measure (e.g. model skill score) and one absolute error measure (e.g. RMSD) with additional supporting information. For this deployment, a model skill score of 0.93 was computed. This is higher than model skill computed in other comparable studies (e.g. Refs. [46,47]).

Snapshots of the vertical velocity profile from ADCP data and the EFDC model are shown in Fig. 4(b). Note that ADCP data are not available for depths less than about 4 m from the sediment bed. Also, near the water surface, there is some noise in the data. An inherent limitation in ADCP current measurements is near the surface due to side-lobe contamination and near-surface, wind-induced errors [48,49]. Instrumental specifications suggest the depth of contamination to be approximately 15% of the water column [50]. Ignoring these regions, the modelled velocity profiles closely replicate the ADCP data.

These metrics indicate that the model is performing within acceptable bounds in simulating flows within Cobscook Bay. Water level comparisons conducted in July 2004, allowed for calibration of the model against measurements. Results indicate that the model adequately replicates water elevations across the study site with a tendency to over-predict the maximum range. A further validation step that compared model against ADCP measured velocities in 2011 returns a high model skill score and a relative RMSD that is little over 10%. This distinct model calibration (against water level data), model validation (against ADCP data) approach demonstrates that the model replicates flow processes in the bay to a reasonable degree of accuracy.

### 2.3. MHK arrays

The turbine farm considered is composed of ORPCs TidGen™ Power System [51], an installation designed to generate emission-free electricity at tidal and deep river sites. ORPC has a five-turbine array planned for Cobscook Bay; the locations of which are denoted in red in Fig. 5. The core component of the TidGen™ Power System is ORPCs proprietary turbine generator unit (TGU). The TGU utilizes four advanced design cross flow (ADCF) turbines to drive a permanent magnet generator mounted between the turbines on a common driveshaft. The ADCF turbines rotate in the same direction regardless of tidal flow direction; rotational speed of the turbines is directly related to water flow speed. The TGU is 30 m in length, 5.2 m high and 5.2 m wide. It is attached to a bottom support frame, which holds the TGU in place approximately 4.5 m above the sea floor. The coupled TGU and bottom support frame comprise the TidGen™ device.

The support structures are assumed to occupy 3 m of the width and to extend from the sediment bed to 11.2 m height. Thrust coefficients are specified as $C_T = 0.8$ and drag coefficients for the support structures are $C_S = 1.2$. We chose a relatively high thrust coefficient to be environmentally conservative; because physical environmental changes are expected to increase as more energy is removed from the tidal channel.

Because the turbines occupy only a fraction of a cell (30-m turbine in a 100-m cell), some discussion of the model

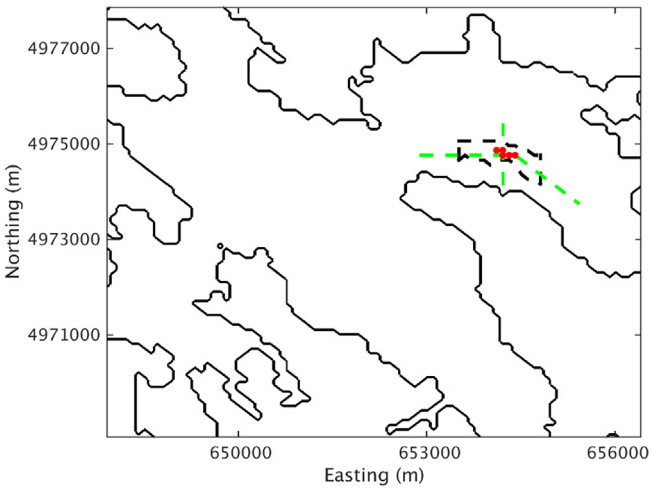


**Fig. 5.** Outline map of the MHK turbine locations (red circles), position of aquaculture farm (dashed black line) and location for which vertical profiles of velocity are presented in east-west and north-south direction. (For interpretation of the references to colour in this figure legend, the reader is referred to the web version of this article.)

implementation is warranted. Power removed by a turbine is calculated as [52,53].

$$P = \frac{1}{2} C_T \rho A_T U^3, \tag{3}$$

where $\rho$ is the fluid density, $U$ is the velocity, and $A_T$ is the flow-facing area of the MHK turbine. It is assumed that the turbine is always aligned with the flow direction (although this may be impossible in a three-dimensional, bi-direction flow). From the power equation, the local force applied on the water column is [52,53].

$$F = \frac{P}{U} = \frac{1}{2} C_T \rho A_T U^2. \tag{4}$$

Given this formulation and the known turbine area, model-calculated velocities are used to specify the force applied to the flow by the MHK device. This force is decomposed into vector components based on the directional velocity components. Area-weighted forces are then applied to each vertical face of the model cell in which the MHK (or support) resides. If the MHK device occupies only a portion of a vertical (sigma) model layer, appropriate weighting is applied. An analogous computation applies for the MHK support structures where $C_T$ is replaced by $C_S$. The five ORPC turbines removed about 136 MW-hr over the 30-day simulation (July 2010 simulation). The support structures dissipated about an additional 10 MW-hr over the same time period.

### 2.4. Aquaculture installations

The method of growing shellfish by suspension culture is a long-established and important industry. This cultivation method involves lowering bivalves into the water column on ropes, called droppers, suspended from flotation units, which usually consist of rafts or longlines [54,55]. These installations form a suspended canopy that act as distributed drag elements that collectively yield a porous obstacle to flow. Field studies have demonstrated that suspended canopies alter ambient flows in a number of ways including amended current speeds and direction within the canopy, and increased flows beneath and around the canopy [7,8,54]. Fig. 6 presents an idealised flow profile within a suspended canopy configuration that illustrates the effects and the associated potential for renewable energy exploitation that takes advantage of flow acceleration beneath the canopy.

In this study, the effects of the rope dropper installations were simulated as an additional drag term included in the governing equations. The aquaculture force was applied to the upper portion of the water column to simulate a suspended canopy and can be expressed as

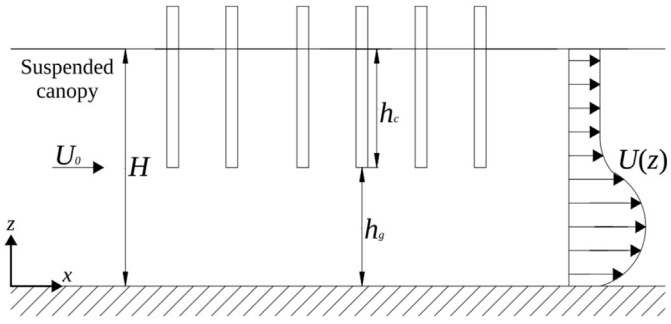


**Fig. 6.** Diagram for a suspended canopy configuration demonstrating the associated flow profile. $H$ is the water depth; $h_g$ the gap beneath the canopy; $h_c$ the height of the canopy; and $U_0$ the depth-averaged velocity. The idealised flow profile within the canopy, $U(z)$, illustrates the amended flow scheme induced by the canopy, and suggests where to place tidal stream turbines to take advantage of accelerated flows.

$$F_D = \frac{1}{2} a C_D U \sqrt{U^2 + V^2}, \tag{5}$$

where $a$ is projected area of canopy per unit volume, $C_D$ is the drag coefficient, and $F_D$ is the drag per unit fluid mass.

Specification of an appropriate value of drag coefficient is important for accurate parameterisation of canopy flow processes. Factors influencing the characterisation of drag coefficient include flow conditions, canopy density, and the shape of the canopy elements. Increased dropper density decreases both flow and Reynolds number, $Re$, and thus, based on the relationship between drag and $Re$ for an idealised cylinder, a larger drag coefficient is required [56]. Furthermore, drag is not constant along the length of a cylinder with wake disturbances and vortex formation having been observed [57].

This study adopts a canopy drag coefficient that varies both as a function of canopy density, and also vertically along the length of the dropper elements. The model implements a drag coefficient that decreases with increasing cylinder density ($ad$), according to the best fit polynomial derived by Ghisalberti and Nepf [58]:

$$C_{DA} = \frac{C_{DC}}{1.16}\left[1.16 - 9.31(ad) + 38.6(ad)^2 - 59.8(ad)^3\right], \tag{6}$$

where $d$ is the canopy element diameter, $C_{DC}$ is the drag coefficient of an isolated, infinite cylinder, and $C_{DA}$ is the bulk drag coefficient of an array of cylinders. Moreover, the vertical profile of the density-dependent drag coefficient defined above was further adjusted based on a detailed comparison with experimental data [11,59], and can be expressed as

$$C_D = C_{DA}\left[1.05 - 0.4\left(\frac{z}{h_c}\right)^{4.49}\right]. \tag{7}$$

Hence, $C_D$ can vary both spatially across each model cell and vertically across sigma layers depending on the density of canopy ($ad$) and vertical position within the canopy $\frac{z}{h_c}$.

For this study, an aquaculture farm was placed near the same location as the turbine arrays described previously. The farm was assumed to be typical of European configurations with a canopy density of 0.068 $m^{-1}$ and individual droppers having an average diameter of 0.16 m [9,60,61]. The farm extended across an area 1.4 km long and 1.0 km wide. The farm design serves as a representative study of the effects on MHK-device energy production capacity and is also salient to the study of potential environmental impacts. To that end, droppers were assumed to populate the entire farm area where water depth exceeded 20 m. For practical purposes, canopy installations were constrained to the upper 6 m of the water column to provide sufficient clearance between the farm and MHK devices at all stages of the tidal cycle, which has a maximum range exceeding 7 m.

## 3. Results and discussion

### 3.1. Aquaculture structures

Numerical simulations investigated the effects of the canopy installations on flow processes and material transport. Simulations revealed decreased flows within canopy grid cells and corresponding increases in flow rates beneath and around the canopy. Further, non-local effects were observed, with flow processes altered at considerable distances from the canopy installation. Fig. 7

presents velocity vectors at mid-rising and mid-falling tide within the surface layer. For illustrative purposes, simulated flow fields with canopy in place are overlaid on computed vectors for the undisturbed case. These afford a qualitative study of the effects of canopy installations on flows analysed in greater detail in the remainder of this section.

Fig. 8 presents contour plots of velocities within the outer bay at mid-falling tide. To better assess impacts of aquaculture farms, velocities are depth-averaged over all layers containing aquaculture canopy; hence Fig. 8(a) presents mean velocities over the upper 6 m of the water column at mid-tidal cycle. Maximum flows develop in a narrow region connecting the inner harbour to the open ocean through the tidal boundary condition on the right hand side. Within this region, flows of up to 2 m/s are computed. Fig. 8(b) presents velocity differentials when aquaculture structures are included. The structures impose local flow attenuation of up to 50%, especially at the center of the farm. In conjunction with this, velocities increase outside the farm as flow is diverted around the structures. Some degree of flow acceleration is observed across a wide area in the outer bay, particularly to the north of the installations with greater differentials closer to the farm.

Flow attenuation within the canopies is balanced by flow acceleration either around or beneath them [62,63]. To better understand the relative importance of horizontal and vertical diversion of flows, Fig. 9 presents vertical section of velocity differentials at an equivalent stage of the tidal cycle. The locations chosen for vertical sections are indicated by dashed green lines in Fig. 5. Fig. 9(a) presents a profile in the east-west direction and 9(b) in the north-south. Changes in flow speeds are given as percentage changes relative to the undisturbed case. The solid black rectangle indicates the location of the suspended canopy within the water column. The vertical profiles demonstrate that the impact of the suspended canopy on flows extends beyond the location of the canopy itself. Attenuation of flows is observed at depths of up to 25 m with only a slight acceleration occurring in most of the bay. The exception to this is in the deeper section of the bay in Fig. 9(a) where flow acceleration exceeds 20%. This also serves to highlight the many factors that influence flow development with local bathymetry playing a major role.

The degree of flow attenuation imparted by aquaculture structures is a direct function of the canopy density. In our model, density is represented by $a$, the projected area of the droppers per unit volume and $d$, canopy element diameter. To investigate sensitivity of modelled flows to canopy density, we consider $d$ to be static and assess the effect of varying $a$. The objective of these simulations is to determine the optimal density of the canopy installation to maximise MHK production capacity. That is, we aim to minimise the attenuation of flow induced by the canopy while maximising associated flow acceleration within the MHK cells. Fig. 10 presents flow changes within the farm and MHK cells, respectively, as the canopy density changes. Farm current speeds are averaged horizontally and vertically over model cells and layers containing aquaculture canopies. Likewise for the MHK current speeds, averaging is over model cells and layers containing the five MHK devices. Results demonstrate that at relatively low canopy density, average flows in the MHK cells reach a maximum. Flow speeds increase with increasing density up to a value of approximately 0.04 $m^{-1}$; for density increases beyond this point, no further increase in flow speeds is computed in the MHK cells. These results suggest that the optimal stocking density for this canopy configuration is between 0.02 and 0.04 to maximise MHK production capacity (this does not consider operation of the aquaculture farm itself to promote optimal growth rates and manage impacts on the physical environment). In practice, densities can vary from values as low as 0.03 for longline configurations [9] up to 0.3 for the denser, raft-type configurations [54].

The effects of the aquaculture canopies on material transport and residence times were also examined. Transport time scales of both the entire bay and the aquaculture region in isolation were investigated. To investigate the flushing characteristics of the bay, the model was run until steady-state conditions were achieved (c. 5 days). The entire bay was then specified as having a uniform initial concentration of tracer, $C_0$ that decays with time as dye is flushed out of the bay each tidal cycle. Fig. 11 presents the dye decay curve for Cobscook Bay with and without aquaculture. Fig. 11(a) compares tracer decay curves over the full 30-day simulation, while Fig. 11(b) presents the percentage difference between scenarios. As expected, aquaculture does not significantly affect material transport in the bay primarily due to the relatively small spatial extent of the installation. Percent differences are typically less than 2% with

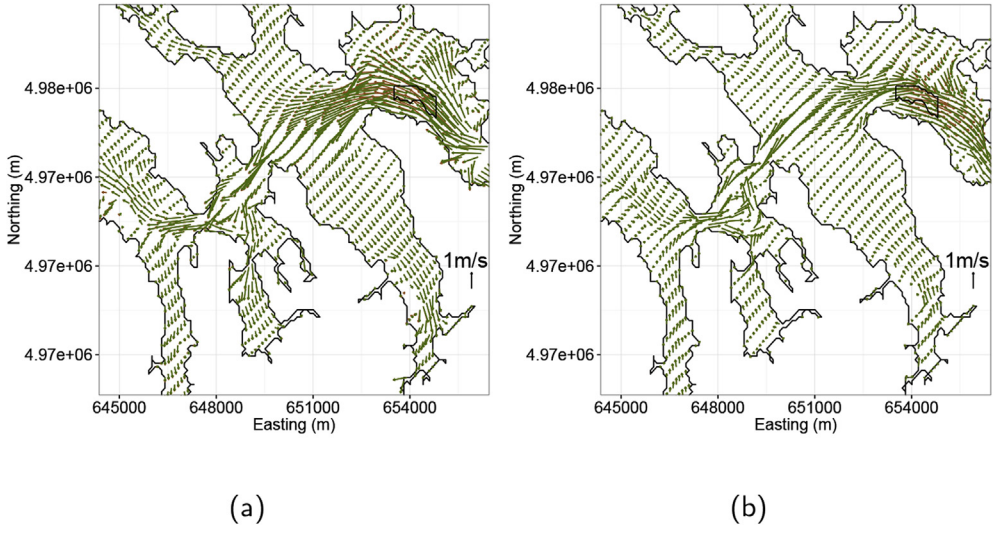


**Fig. 7.** Modelled velocity vectors at mid-rising tide (LHS) and mid-falling tide (RHS) within Cobscook Bay. For illustrative purposes, model simulated flow fields with (green vectors) and without (brown vectors) aquaculture installations are presented. Attenuation of current speeds is evident within the aquaculture footprint indicated by the black polygon. (For interpretation of the references to colour in this figure legend, the reader is referred to the web version of this article.)

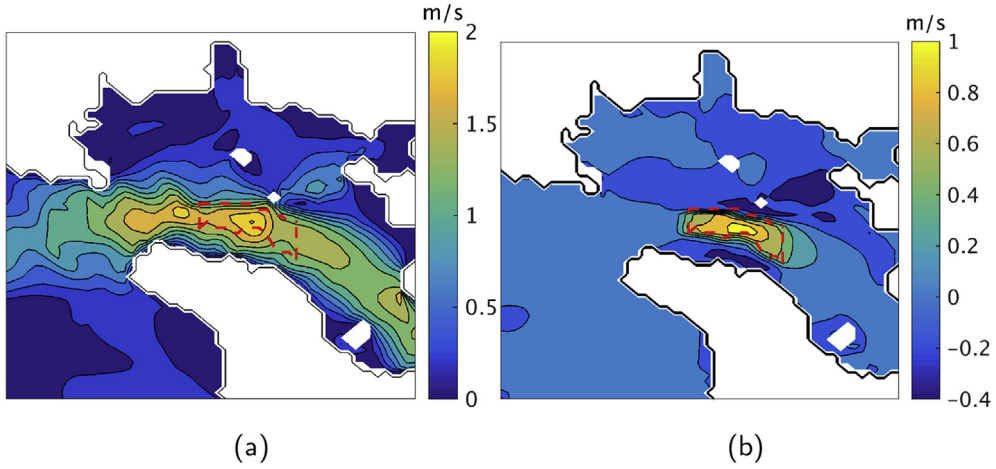


**Fig. 8.** Synoptic snapshot of modelled current speeds (m/s) at mid-tidal cycle within the outer bay for (a) undisturbed case and (b) differences in current speeds as a result of aquaculture canopies. Velocities are depth-averaged across all layers containing aquaculture canopy and differentials are computed relative to the benchmark, no aquaculture configuration (i.e., negative differentials indicate acceleration of flow around the aquaculture installation).

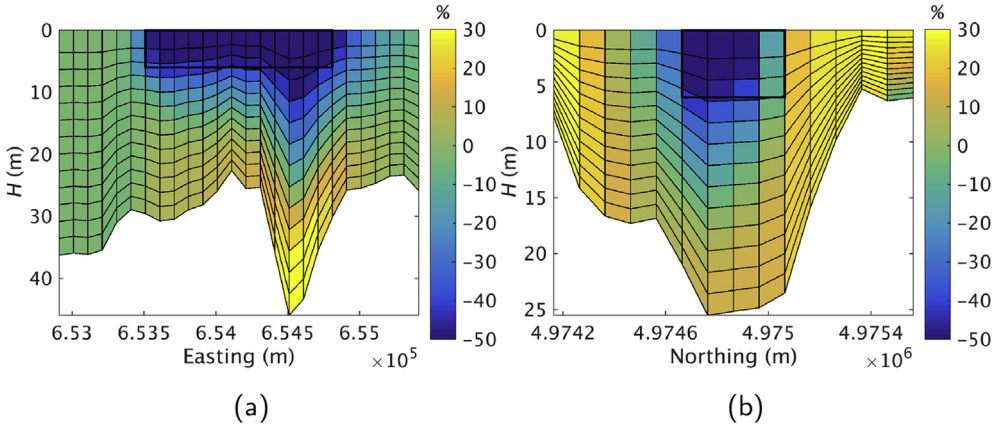


**Fig. 9.** (a) East-west and (b) north-south vertical sections through the aquaculture farm showing the changes in flow speeds resulting from aquaculture installation. Flow differentials are presented as percentage change relative to the undisturbed case.

values higher after multiple days of simulations due largely to the retained values being small and hence relative differences becoming more sensitive.

Secondly, we focused on material transport time scales within the aquaculture farms, specifically on the pulse residence times (PRT) of the aquaculture site, which were defined by Miller and McPherson [64], as the time to flush a given fraction (e.g., 95%) of a conservative tracer/dye from a water body after introduction within the aquaculture footprint (or other given location) [65]. showed that PRT provide a measure of the self-purification capacity of an aquaculture site due to tidal exchange with the outer sea and turbulent dispersion. Fig. 12 presents details on the time required to flush 95% of a conservative constituent from the aquaculture cells. Tracer concentrations are depth-averaged over all layers containing canopy installations (top 6 m of the water column). Fig. 12(a) presents the spatial distribution of time in hours to flush 95% of the tracer from the farm region with no aquaculture installation, while Fig. 12(b) presents the equivalent metric incorporating aquaculture drag. Fig. 12(c) presents the changes in flushing time due to aquaculture (in hours), while Fig. 12(d) presents the relative increases in flushing resulting from aquaculture.

The region demonstrates low flushing time scales, primarily due to the exposed location of the site, subject to large tidal effects. Flushing is less than 40 h for the entire area, with aquaculture drag amending these times considerably. Results demonstrate that even for such a relatively small-scale farm development, flushing times are increased by 10–20% within its footprint. These results demonstrate that canopies can impact both current speeds and material transport. The effects on material transport are predominantly local, with the impact on bay-scale flushing negligible. In the next section, we consider the effects of MHK devices on hydrodynamics.

### 3.2. MHK arrays

This section focuses on the effects of MHK-device drag on flows. Numerical simulations incorporate the five-turbine array as described in Methodology. Fig. 13 presents the effects of the MHK devices on current speeds with 13(a) quantifying percent changes in horizontal flows at a single model layer containing MHK devices. Reductions in water speed of up to 10% occur inside the MHK array with modest acceleration in surrounding cells. In general, flow acceleration of 2–4% is computed across much of the outer bay. Isolated regions of higher relative flow changes are observed, due to

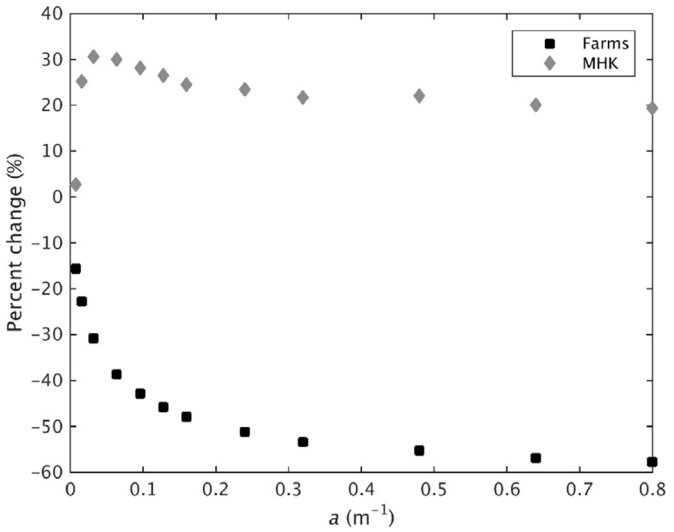


**Fig. 10.** Changes in current speeds at mid-tidal-cycle within the farm and MHK regions as a function of canopy density. Canopy current speeds (squares) are averaged horizontally and vertically over model cells and layers that contain aquaculture. Likewise for the MHK current speeds, averaging is over the cells and layers containing the five MHK devices.

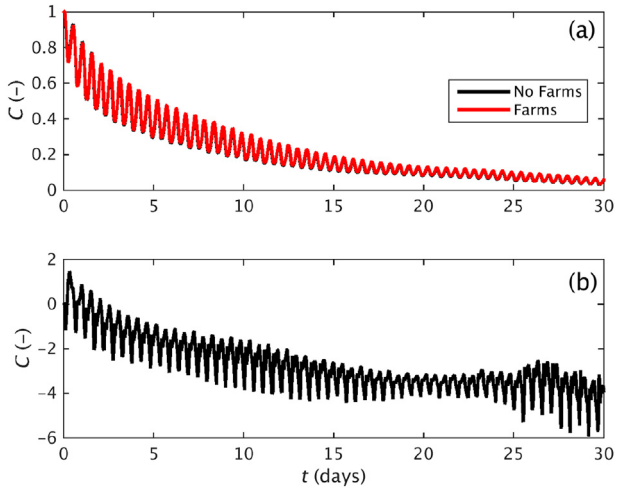


**Fig. 11.** Decay curves of (a) the average dye concentration in Cobscook Bay with and without aquaculture installations and (b) % change in dye concentration due to farm drag.

low ambient flows in certain shallow cells (e.g., in vicinity of islands) yielding increased sensitivity to flow changes. Fig. 13(b) presents a vertical profile of flows demonstrating a reduction of current speeds in model cells containing MHK turbines with slight acceleration in the overlying layers. Local to the MHK cells, flow attenuation of up to 20% is reported while maximum flow acceleration is about 5%.

In general, effects on flows are not as significant as observed for the aquaculture installations, due primarily to the smaller spatial coverage. The aquaculture farm encompasses a horizontal area of 750,000 m$^2$ while the MHK installation, at 50,000 m$^2$, is a factor of ten smaller. Flow amendment is generally localised to model cells and layers containing MHK devices with only moderate impacts in neighbouring regions. Averaging velocities vertically and over the five model cells containing MHK devices, the resultant change in current speeds is less than 3% at mid-stage of the tidal cycle, corresponding to flow changes of less than 5 cm/s.

### 3.3. Multi-use facilities combining aquaculture and MHK resources

Previous sections have demonstrated that the suspended canopy and MHK installations impact the physical environment to varying degrees. Further, simulations showed that canopy installations have potential to increase renewable energy production capacity by increasing flows near the locations of the turbines. However, information on the effects of these installations deployed in combination is critical to begin to understand the viability of the approach. This section presents numerical simulations investigating the effects of combined aquaculture farms and MHK devices on flows and material transport in the bay.

Fig. 14 presents changes to flow speeds resulting from the installations. Flows are depth averaged and velocity differentials at two stages of the tidal cycle are computed, namely mid-flood and mid-ebb. Changes to flow speed of up to 0.4 m/s are computed. In addition, the effects of the installations extend a considerable distance beyond the extents of the structures. Particularly on the flood tide, flow attenuation is reported some distance into the inner bay, while diversion of flow increases current speeds across a large area to the north of the installations.

Fig. 15(a) presents vertical sections quantifying the change in velocity due to the installations. Results demonstrate that the vertical profile is quite similar to the case where only suspended canopies are included (Fig. 9). In general, flows decrease rapidly within the canopy coupled with some degree of acceleration beneath and around the canopy. The reduction in flow speeds within MHK cells is less than for the MHK alone deployments (relative to free-stream flows). Fig. 15(b) presents the difference in flows when both aquaculture and MHK forces are included as opposed to only the suspended canopy drag. In some cells, the MHK arrays reduces flow speeds by up to 15% relative to the aquaculture installations on their own. The additional MHK force reduces flow diversion beneath the canopy with some further attenuation occurring within the canopy above the MHK devices. This results from the combined aquaculture and turbine farms increasing horizontal diversions around the farm relative to the aquaculture only case.

Finally, we investigate the energy generating capacity of the system incorporating both aquaculture and MHK installations. Fig. 16 presents a synoptic profile of zonal velocities at four of the five proposed MHK device locations. The plot provides insight into potential flow acceleration that might develop beneath the aquaculture canopies and could be exploited for energy generation by the MHK devices. Vertical velocity profiles are presented for four cases: undisturbed flows, aquaculture canopies only, MHK devices only, and finally both aquaculture canopies and MHK devices denoted by the red curves. Velocity profiles incorporating only aquaculture canopies demonstrate a clear acceleration of flow beneath the canopy. The vertical position at which velocity reaches a maximum is critical for optimising energy production capacity. Undisturbed vertical velocity profiles follow the expected boundary-layer profile. Inclusion of aquaculture complicates the vertical flow profile with maximum velocities occurring where the shear effects of both the canopy and bed are minimum. The point at which this maximum occurs is a function of canopy height, density, and the depth of the water column. In particular, the height of the gap between the canopy and ocean floor is of primary importance. Fig. 16 demonstrates that at all four sites, the presence of the canopy increases velocities at the proposed location of the turbine. The increase is most pronounced for Fig. 16(d) where the deeper water in that region allows for flow acceleration to coincide with the

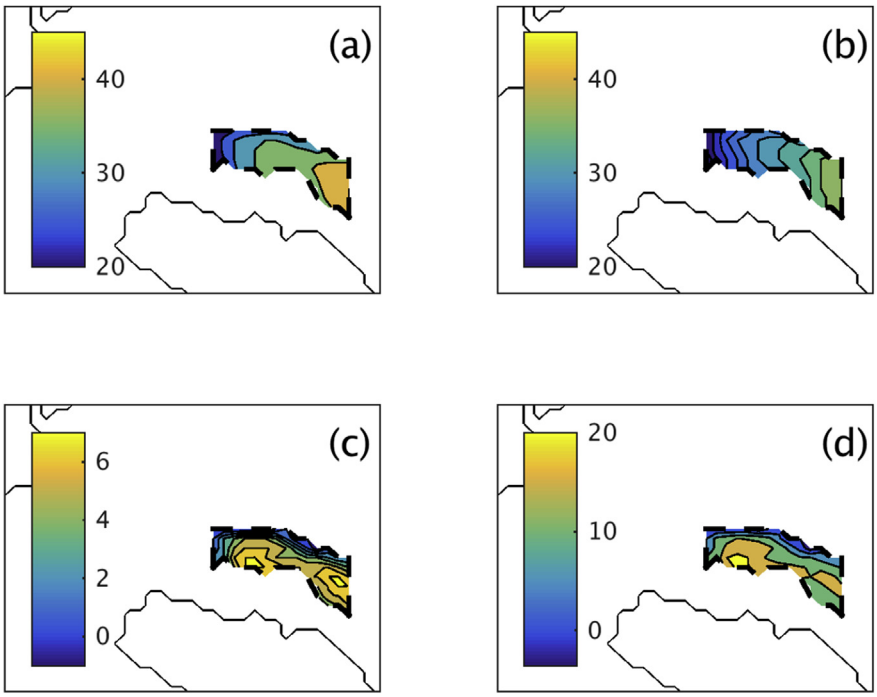


**Fig. 12.** PRT 95% (the time to flush 95% of conservative tracer) in hours for (a) no aquaculture farms and (b) aquaculture installations included. The bottom figures present (c) differences in flushing time (hours) and (d) % change in flushing time due to aquaculture farms with positive values indicating increased flushing times due to the farm drag.

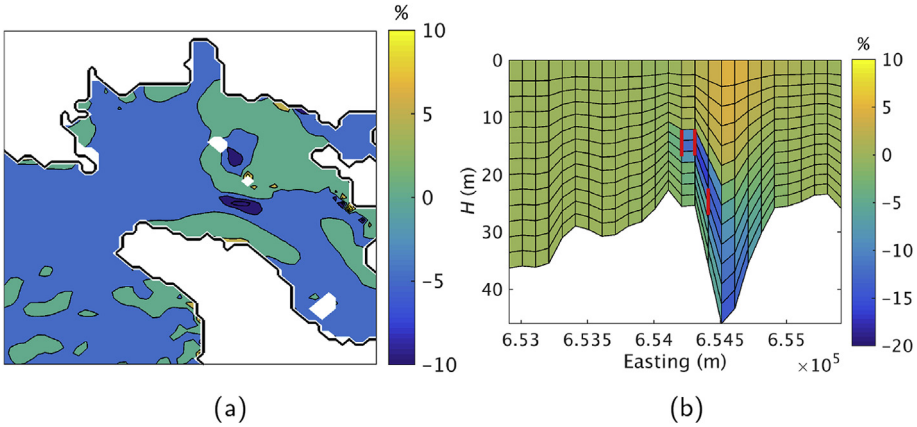


**Fig. 13.** (a) Percentage change in current speeds due to MHK-device installation at mid-tidal cycle. Velocities are computed at model layers in which MHK devices are present. (b) Vertical section showing the amendment to flow resulting from MHK-device installation. Flow differentials are presented as percentage changes while the red dots indicate the locations of MHK devices within the water column.

location of the MHK device.

Clear opportunities exist to convert this increase in flow speeds to an increase in energy production capacity. Equation (3) presents the power extracted by an MHK turbine as a function of flow speed. We computed the energy produced by the five proposed MHK devices over a full tidal cycle for comparison to the undisturbed case. Flow speeds were averaged over the model layers containing a MHK device to provide a representative velocity. The ORPC TidGen™ turbine discussed in this study has an operational cut-in speed of 1 m/s (i.e., it only generates power when flows are greater than this value). To provide a more representative quantification of energy generation, we compute energy output for each turbine subject to this threshold.

Table 1 presents the energy production capacity in the model cells containing each turbine for the four different configurations (undisturbed, aquaculture canopies, MHK devices, and both aquaculture canopies and MHK devices). The final row summarises these metrics in terms of total energy generating capacity of the different configurations relative to the undisturbed case (i.e., a value of 1.0 is ascribed). The amended model configurations notably impact energy production capacity. The MHK devices reduce energy production capacity by 25% relative to undisturbed flows. The large impact of the MHK devices is expected because the fundamental design of these devices is based on extracting energy from flows for conversion to electricity. Including canopy structures increases the production capacity of the model cells to values close to those computed assuming flow speeds remain unchanged by the MHK devices. Across the five locations, production capacity is 5% greater than values computed assuming no additional induced drag. If we consider the case with no structures in place as a

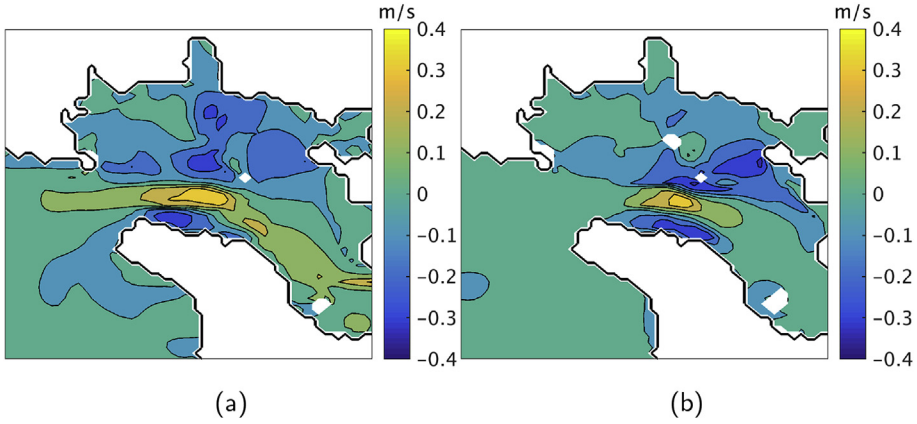


**Fig. 14.** Changes in current speeds due to aquaculture and MHK installations on flood (a) and ebb (b) tides. Velocities are depth-averaged across all layers and differentials are computed relative to the undisturbed case.

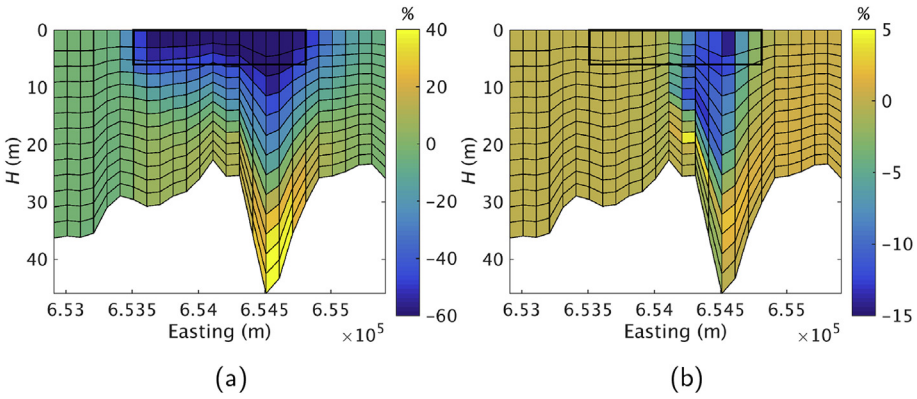


**Fig. 15.** Vertical sections quantifying percentage flow changes resulting from the combined aquaculture and MHK installations. Changes relative to the undisturbed case is presented in (a) while (b) shows percentage changes between simulations incorporating aquaculture drag only and incorporating both aquaculture and MHK forces.

benchmark of energy generating capacity then Table 1 indicates that for this configuration there is a potential to increase production capacity by 19% due to the effects of the aquaculture installation. In other words, the flow acceleration beneath the aquaculture installation is such as to potentially increase MHK energy production capacity by 19% across the five turbines. This is supported by analysis of Fig. 16 which indicates the inclusion of the canopy increases flows noticeably in the cells containing the MHK devices. Considering that energy generation is a function of velocity cubed, the potential for increased production capacity is clear.

## 4. Conclusions

A numerical model of Cobscook Bay was developed and calibrated to serve as a test bed to simulate the potential changes to local and regional hydrodynamics for aquaculture and/or MHK installations. The model faithfully represented water levels collected at three NOAA stations. Velocities collected from an ADCP were also simulated with somewhat greater variability in agreement metrics. Using the validated model, the influence of suspended aquaculture canopies was investigated with regard to local flow changes, regional dye concentration decays (as a surrogate for flushing rate), and local pulse residence times. Although local flow changes were amended, overall bay flushing rates were decreased by no more than 6%. Flow profiles in the footprint of the aquaculture farm indicated decreased flow speeds through the canopy and increased flow speeds beneath and around the canopy. A similar analysis of changes to the local flows near five MHK devices was also conducted. Again, decreased flow speeds were observed local to the MHK devices, but these changes did not extend more than a few model cells (100s of meters) away. In an effort to study the potential synergies between aquaculture and MHK energy production, the MHK devices were placed below the aquaculture canopy in the region of accelerated flow. Increases in energy production of up to 19% were noted. Finally, the energy fluxes through model cells containing MHK devices were analysed for the various configurations (i.e., undisturbed, canopy only, MHK only, and combined canopy and MHK). Presence of the aquaculture canopy increased the energy flux through the model cells where MHK devices were to be located. Moreover, while the MHK devices sharply decreased energy fluxes through the model cells in which they were present. It was notable that the combination of aquaculture canopy and MHK devices actually increased the energy flux through these model cells. This research investigates suspended aquaculture installations co-located with MHK devices within a designated tidal energy test site. Certain aspects of the study are specific to this site (e.g. quantified energy production capacity, transport time scales, etc.). However, findings from this paper can be extended to other sites. In particular, we demonstrate the viability of co-locating suspended aquaculture installations with MHK devices to increase energy production capacity of the turbines.

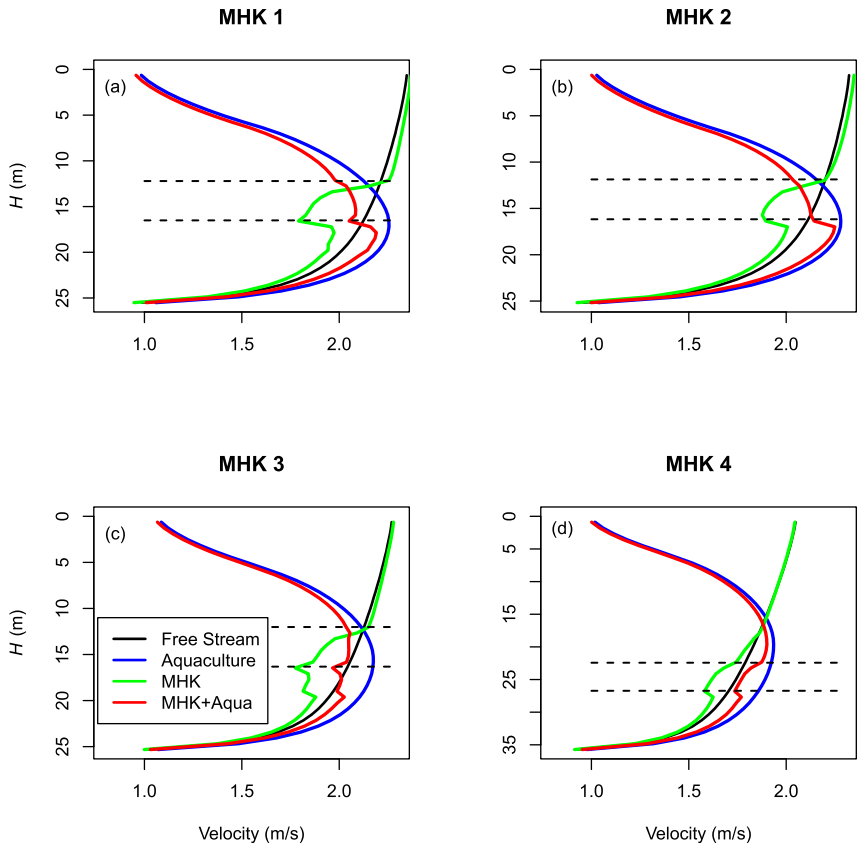


**Fig. 16.** Vertical velocity profiles at four MHK locations demonstrating the effects of the additional forces on flows at mid-tidal cycle. The four curves represent configurations for the undisturbed case (black curves), with the suspended aquaculture canopy (blue curves), with the MHK device (green curves), and the combined aquaculture canopy and MHK device (red curves). The dashed black lines indicate the locations of the MHK devices in the water column. (For interpretation of the references to colour in this figure legend, the reader is referred to the web version of this article.)

**Table 1**
Energy production capacity at model cells containing MHK devices subject to different physical drag configurations. Column 2 presents computed energy generation potential for undisturbed flows, while columns 3, 4, and 5 present computed energy generation potential subject to the effects of the aquaculture canopy, the MHK device, and the combined impacts of the aquaculture and MHK device, respectively. The final row presents the total relative energy generation capacity of the five MHK devices.

| Turbine − | Free stream (MW-hr) | Aquaculture (MW-hr) | MHK (MW-hr) | MHK + Aqua (MW-hr) |
|---|---|---|---|---|
| MHK 1 | 1.01 | 1.60 | 0.79 | 1.43 |
| MHK 2 | 1.77 | 1.97 | 1.28 | 1.78 |
| MHK 3 | 2.06 | 2.27 | 1.49 | 2.02 |
| MHK 4 | 1.96 | 2.33 | 1.50 | 2.07 |
| MHK 5 | 1.85 | 2.12 | 1.35 | 1.81 |
| Relative energy | 1 | 1.19 | 0.74 | 1.05 |

## References


[1] FAO, The State of the World Fisheries and Aquaculture, in: Tech. Rep., Food and Agriculture Organization of the United Nations, 2014.
[2] J.D. Sachs, The promise of the blue revolution, Sci. Am. 297 (1) (2007) 37–38.
[3] B.H. Buck, M.W. Ebeling, T. Michler-Cieluch, Mussel cultivation as a co-use in offshore wind farms: potential and economic feasibility, Aquac. Econ. Manag. 14 (4) (2010) 255–281.
[4] B.H. Buck, G. Krause, T. Michler-Cieluch, M. Brenner, C. Buchholz, J. Busch, R. Fisch, M. Geisen, O. Zielinski, Meeting the quest for spatial efficiency: progress and prospects of extensive aquaculture within offshore wind farms, Helgol. Mar. Res. 62 (3) (2008) 269–281.
[5] T. Michler-Cieluch, G. Krause, B.H. Buck, Marine aquaculture within offshore wind farms: social aspects of multiple-use planning, GAIA-Ecological Perspect. Sci. Soc. 18 (2) (2009) 158–162.
[6] T. Michler-Cieluch, G. Krause, B.H. Buck, Reflections on integrating operation and maintenance activities of offshore wind farms and mariculture, Ocean. Coast Manag. 52 (1) (2009) 57–68.
[7] J. Blanco, M. Zapata, A. Morono, Some aspects of the water flow through mussel rafts, Sci. Mar. 60 (2–3) (1994) 275–282.
[8] D.R. Plew, C.L. Stevens, R.H. Spigel, N.D. Hartstein, Hydrodynamic implications of large offshore mussel farms, IEEE J. Ocean. Eng. 30 (1) (2005) 95–108.
[9] F. O'Donncha, M. Hartnett, S. Nash, Physical and numerical investigation of the hydrodynamic implications of aquaculture farms, Aquacult. Eng. 52 (2013) 14–26, http://dx.doi.org/10.1016/j.aquaeng.2012.07.006.
[10] J. Hamrick, A Three-dimensional Environmental Fluid Dynamics Computer Code: Theoretical and Computational Aspects, in: Tech. Rep., Virginia Institute of Marine Science, 1992.
[11] F. O'Donncha, M. Hartnett, D.R. Plew, Parameterizing suspended canopy effects in a three-dimensional hydrodynamic model, J. Hydraul. Res. 53 (6) (2015) 714–727, http://dx.doi.org/10.1080/00221686.2015.1093036.
[12] F. O'Donncha, S.C. James, N. O'Brien, E. Ragnoli, Numerical modelling study of the effects of suspended aquaculture farms on tidal stream energy generation, in: OCEANS, 2015, Genova, Italy, 2015, pp. 1–7.
[13] S.C. James, C.A. Jones, M.D. Grace, J.D. Roberts, Advances in sediment transport modelling, J. Hydraul. Res. 48 (6) (2010) 754–763.
[14] S.C. James, E. Seetho, C. Jones, J. Roberts, Simulating environmental changes due to marine hydrokinetic energy installations, in: OCEANS, 2010, Seattle, Washngton, 2010, pp. 1–10.
[15] S.C. James, J. Barco, E. Johnson, J. Roberts, S. Lefantzi, Verifying marine-hydrokinetic energy generation simulations using SNL-EFDC, in: OCEANS, 2011,

Kona, Hawaii, 2011, pp. 1–9.
[16] S.C. James, J. Roberts, Sandia National Laboratories Environmental Fluid Dynamics Code: Marine Hydrokinetic Module User's Manual, in: Tech. Rep. SAND2014-1804, Sandia National Laboratories, Albuquerque, Livermore, CA, 2014.
[17] J.M. Hamrick, User's Manual for the Environmental Fluid Dynamics Computer Code, in: Tech. Rep., Virginia Institute of Marine Science, 1996.
[18] Z.G. Ji, M.R. Morton, J.M. Hamrick, Wetting and drying simulation of estuarine processes, Estuar. Coast Shelf S 53 (2001) 683–700.
[19] G.L. Mellor, T. Yamada, Development of a turbulence closure model for geophysical fluid problems, Rev. Geophys. Space Phys. 20 (4) (1982) 851–875.
[20] B. Galperin, L.H. Kantha, S. Hassid, A. Rosati, A quasi-equilibrium turbulent energy model for geophysical flow, J. Atmos. Sci. (1988) 55–61.
[21] J. Smagorinsky, General circulation experiments with the primitive equations, part I: the basic experiment, Mon. Wea. Rev. 91 (3) (1963) 99–164.
[22] F. O'Donncha, E. Ragnoli, F. Suits, Parallelisation study of a three-dimensional environmental flow model, Comput. Geosci. 64 (2014) 96–103.
[23] F. O'Donncha, S.C. James, N. O'Brien, E. Ragnoli, Parallelisation of hydro-environmental model for simulating marine current devices, in: OCEANS, 2015, Washington D.C, 2015, pp. 1–7.
[24] F. O'Donncha, E. Ragnoli, S. Venugopal, S.C. James, K. Katrinis, On the efficiency of executing hydro-environmental models on cloud, Proced. Eng. 154 (2016) 199–206, http://dx.doi.org/10.1016/j.proeng.2016.07.447.
[25] F. O'Donncha, S. Venugopal, S.C. James, E. Ragnoli, Deploying and optimizing performance of a 3D hydrodynamic model on Cloud, in: OCEANS, 2016, Monterey, California, 2016, pp. 1–7.
[26] J. Shen, J. Boon, A. Kuo, A modeling study of a tidal intrusion front and its impact on larval dispersion in the james river estuary, Virginia, Estuaries 22 (3) (1999) 681–692.
[27] J.M. Hamrick, Estuarine environmental impact assessment using a three-dimensional circulation and transport model, Estuar. Coast. Model. 2 (1992) 292–303.
[28] S. Bai, W. Lung, Modeling sediment impact on the transport of fecal bacteria, Water Res. 39 (20) (2005) 5232–5240, http://dx.doi.org/10.1016/j.watres.2005.10.013.
[29] P. Thanh, M.D. Grace, S.C. James, Sandia National Laboratories Environmental Fluid Dynamics Code: Sediment Transport User Manual, in: Tech. Rep., SAND2008-5621, 2008. Livermore, CA.
[30] S.C. James, V. Boriah, Modeling algae growth in an open-channel raceway, J. Comput. Biol. 17 (7) (2010) 895–906.
[31] S.C. James, V. Janardhanam, D.T. Hanson, Simulating PH effects in an algal-growth hydrodynamics model, J. Phycol. 49 (3) (2013) 608–615.
[32] T. Khangaonkar, Y. Zhaoqing, C. Degasperi, K. Marshall, Modeling hydrothermal response of a reservoir to modifications at a high-head dam, Water Int. 30 (3) (2005) 378–388.
[33] Z. Ji, Hydrodynamics and Water Quality: Modeling Rivers, Lakes, and Estuaries, John Wiley & Sons, 2008.
[34] D. Xu, H. Xue, A numerical study of horizontal dispersion in a macro tidal basin, Ocean. Dynam. 61 (5) (2011) 623–637.
[35] V. Panchang, G. Cheng, C. Newell, Modeling hydrodynamics and aquaculture waste transport in coastal Maine, Estuaries 20 (1) (1997) 14–41.
[36] D. Brooks, M. Baca, Y.-T. Lo, Tidal circulation and residence time in a macro-tidal estuary: Cobscook bay, Maine, Estuar. Coast. Shelf Sci. 49 (5) (1999) 647–665.
[37] D.O. Neander, NOAA's Hydrographic Survey Program Northewest Region Update, in: Tech. Rep., NOAA, 2010.
[38] J. Nycander, K. Döös, Open boundary conditions for barotropic waves, J. Geophys. Res-Oceans, 108 (C5).
[39] J. Zhou, S. Pan, R.A. Falconer, Effects of open boundary location on the far-field hydrodynamics of a severn barrage, Ocean. Model 73 (2014) 19–29.
[40] NOAA, Center for Operational Oceanographic Products and Services, January 2016. http://tidesandcurrents.noaa.gov/gmap3/.
[41] D. Xu, H. Xue, D.A. Greenberg, A numerical study of the circulation and drifter trajectories in Cobscook Bay, in: 9th International Conference on Estuarine and Coastal Modeling, 2006, pp. 176–195, http://dx.doi.org/10.1061/40876(209)11.
[42] S. Rao, H. Xue, M. Bao, S. Funke, Determining tidal turbine farm efficiency in the western passage using the disc actuator theory, Ocean. Dynam. 66 (1) (2016) 41–57.
[43] R. McCuen, W. Snyder, A proposed index for comparing hydrographs, Water Resour. Res. 11 (6) (1975) 1021–1024.
[44] C. Willmott, On the validation of models, Phys. Geogr. 2 (C5) (1981) 184–194.
[45] D.R. Legates, G.J. McCabe, Evaluating the use of goodness-of-fit measures in hydrologic and hydroclimatic model validation, Water Resour. Res. 35 (1) (1999) 233–241.
[46] J.C. Warner, W.R. Geyer, J.A. Lerczak, Numerical modeling of an estuary: a comprehensive skill assessment, J. Geophys. Res. 110 (C05001) (2005) 1–13.
[47] F. O'Donncha, M. Hartnett, S. Nash, L. Ren, E. Ragnoli, Characterizing observed circulation patterns within a bay using HF radar and numerical model simulations, J. Mar. Syst. 142 (2015) 96–110.
[48] G. Marmorino, Z. Hallock, On estimating wind velocity using an upward-looking ADCP, J. Atmos. Ocean. Technol. 18 (5) (2001) 791–798.
[49] C. Teague, J. Vesecky, Z. Hallock, A comparison of multifrequency HF radar and ADCP measurements of near-surface currents during COPE-3, IEEE J. Ocean. Eng. 26 (3) (2001) 399–405.
[50] H.-H. Essen, On the capability of an upward-looking ADCP deployed in the Iceland-Faeroe frontal area, Dtsch. Hydrogr. Z. 46 (3) (1994) 211–228.
[51] A.S. Bahaj, Marine current energy conversion: the dawn of a new era in electricity production, Philos. T. Roy. Soc. A 371 (1985) (2013) 20120500.
[52] C. Garrett, P. Cummins, The power potential of tidal currents in channels, P. Roy. Soc. Lond. A. Mat. 461 (2060) (2005) 2563–2572.
[53] C. Garrett, P. Cummins, The efficiency of a turbine in a tidal channel, J. Fluid Mech. 588 (2007) 243–251.
[54] A.J. Boyd, K.G. Heasman, Shellfish mariculture in the Benguela System: water flow patterns within a mussel farm in Saldanha Bay, South Africa, J. Shellfish Res. 17 (1) (1998) 25–32.
[55] C. Stevens, D.R. Plew, N. Hartstein, D. Fredriksson, The physics of open-water shellfish aquaculture, Aquacult. Eng. 38 (3) (2008) 145–160.
[56] W. Wu, S.S.Y. Wang, A depth-averaged two-dimensional numerical model of flow and sediment transport in open channels with vegetation, in: Riparian Vegetation and Fluvial Geomorphology, American Geophysical Union, 2004, pp. 253–265, http://dx.doi.org/10.1029/008WSA18.
[57] T. Kawamura, M. Hiwada, T. Hibino, I. Mabuchi, M. Kumada, Flow around a finite circular cylinder on a flat plate, Bull. JSME 27 (232) (1984) 2142–2151.
[58] M. Ghisalberti, H.M. Nepf, The limited growth of vegetated shear layers, Water Resour. Res. 40 (7) (2004) 1–12.
[59] S.C. James, F. O'Donncha, D.R. Plew, Calibration of a 3D hydrodynamic aquaculture model, in: OCEANS, 2016, Monterey, California, 2016, pp. 1–7.
[60] D.R. Plew, Shellfish farm-induced changes to tidal circulation in an embayment, and implications for seston depletion, Aquac. Environ. Interact. 1 (2011) 201–214.
[61] S. Delaux, C. Stevens, S. Popinet, High-resolution computational fluid dynamics modelling of suspended shellfish structures, Environ. Fluid. Mech. 11 (4) (2011) 405–425.
[62] M.M. Gibbs, M.R. James, S.E. Pickmere, P.H. Woods, B.S. Shakespeare, H.W. Hickman, J. Illingworth, Hydrodynamic and water column properties at six stations associated with mussel farming in Pelorus Sound, New Zeal, J. Mar. Fresh. 25 (3) (1991) 239–254.
[63] D.R. Plew, R.H. Spigel, C.L. Stevens, R.I. Nokes, M.J. Davidson, Stratified flow interactions with a suspended canopy, Environ. Fluid. Mech. 6 (6) (2006) 519–539.
[64] R.L. Miller, B.F. McPherson, Estimating estuarine flushing and residence times in Charlotte Harbor, Florida, via salt balance and a box model, Limnol. Oceanogr. 36 (3) (1991) 602–612.
[65] J.H.W. Lee, K.W. Choi, F. Arega, Environmental management of marine fish culture in Hong Kong, Mar. Pollut. Bull. 47 (1) (2003) 202–210 doi:16/S0025-326X(02)00410-1.